



Analysis of a new geomorphological inventory of landslides in Valles Marineris, Mars



Maria Teresa Brunetti^{a,b,*}, Fausto Guzzetti^a, Mauro Cardinali^a, Federica Fiorucci^a, Michele Santangelo^{a,b}, Paolo Mancinelli^b, Goro Komatsu^c, Lorenzo Borselli^d

^a CNR IRPI, via Madonna Alta 126, 06128 Perugia, Italy

^b Dipartimento di Scienze della Terra, Università degli Studi di Perugia, P.zza dell'Università 1, 06123 Perugia, Italy

^c International Research School of Planetary Sciences, Università "G. d'Annunzio", Viale Pindaro 42, 65127 Pescara, Italy

^d Instituto de Geología, Universidad Autónoma de San Luis Potosí, Av. Dr. Manuel Nava 5, 78240 San Luis Potosí, Mexico

ARTICLE INFO

Article history:

Received 21 March 2013

Received in revised form 5 August 2014

Accepted 15 August 2014

Available online 16 September 2014

Editor: C. Sotin

Keywords:

Mars
landslide mapping
landslide classification
landslide size
landslide mobility
slope stability

ABSTRACT

We completed a systematic mapping of landslides in a 10^5 km^2 area in Tithonium and Ius Chasmata, Valles Marineris, Mars, where landslides are abundant. Using visual interpretation of medium to high-resolution optical images, we mapped and classified the geometry of 219 mass wasting features, including rock slides, complex/compound failures, rock avalanches, debris flows, and rock glacier-like features, for a total landslide area of $A_{LT} = 4.4 \times 10^4 \text{ km}^2$, 44% of the study area, a proportion larger than previously recognised. Studying the landslide inventory, we showed that the probability density of landslide area $p(A_L)$ follows a power law, with a scaling exponent $\alpha = -1.35 \pm 0.01$, significantly different from the exponents found for terrestrial landslides, $\alpha = -2.2$ and $\alpha = -2.4$. This indicates that the proportion of large landslides ($A_L > 10^7 \text{ m}^2$) is larger on Mars than on Earth. We estimated the volume (V_L) of a subset of 49 deep-seated slides in our study area and found that the probability density of landslide volume $p(V_L)$ obeys a power law trend typical of terrestrial rock falls and rock slides, with a slope $\beta = -1.03 \pm 0.01$. From the combined analysis of landslide area and volume measurements, we obtained a power law dependency comparable to a similar relationship obtained for terrestrial bedrock landslides, $V_L = (1.2 \pm 0.8) \times A_L^{(1.25 \pm 0.03)}$. From the fall height H_L and run out length L_L of a subset of 83 slides unaffected by topographic confinement, we obtained the mobility index (Heim's ratio) H_L/L_L , a measure of the apparent friction angle of the failed materials, $\phi = 14.4^\circ \pm 0.4^\circ$. Slope stability simulations and back analyses performed adopting a Limit Equilibrium Method, and using Monte Carlo approaches on failed and stable slopes, suggest that the large landslides in Valles Marineris were seismically induced.

© 2014 Elsevier B.V. All rights reserved.

1. Introduction

On Earth, landslides contribute to shape landscapes in various geological, tectonics, and climatic regions. Besides the Earth, Mars is the planet for which rich information exists on landslides and other mass wasting processes (e.g., Lucchitta, 1978, 1979, 1987; McEwen, 1989; Lucchitta et al., 1992; Shaller and Komatsu, 1994; Quantin et al., 2004a; Soukhovitskaya and Manga, 2006; Bigot-Cormier and Montgomery, 2007; Lucas and Mangeney, 2007). Rainfall, snowmelt, earthquakes, and volcanic activity are the primary natural triggers of terrestrial landslides. The triggers of Martian landslides remain mostly undetermined. Despite the inter-

est of early investigators (Lucchitta, 1978, 1979; McEwen, 1989), and several subsequent studies (e.g., Shaller and Komatsu, 1994; Rossi et al., 2000; Quantin et al., 2004a, 2004b; Soukhovitskaya and Manga, 2006; Bigot-Cormier and Montgomery, 2007; Lajeunesse et al., 2006; Lucas and Mangeney, 2007), no systematic classification and mapping of landslides, and of related mass wasting features, has been performed for Mars. This is surprising, given the abundant geomorphological evidence of slope failures on the planet, and the availability of a wide range of imagery with adequate spatial resolution.

In an attempt to fill this gap, we compiled a geomorphological inventory (Guzzetti et al., 2012) of landslides in Valles Marineris (VM), Mars (Brunetti et al., 2011), adopting the same visual interpretation criteria commonly used by geomorphologists to detect, map, and classify terrestrial landslides over large areas (Rib and Liang, 1978; van Zuidam, 1985; Antonini et al., 2002; Guzzetti et al., 2012). The inventory covers two E-W-striking chasmatas

* Corresponding author at: CNR IRPI, via Madonna Alta 126, 06128 Perugia, Italy.
Tel.: +39 075 501 4408; fax: +39 075 501 4420.

E-mail address: mariateresa.brunetti@irpi.cnr.it (M.T. Brunetti).

(canyons) in the western sector of VM, Tithonium Chasma and Ius Chasma, where slope failures were previously recognised and are known to be abundant (Lucchitta, 1987; McEwen, 1989; Shaller and Komatsu, 1994; Quantin et al., 2004a). The study area covers 10^5 km^2 with elevation in the range from -4500 m to 6200 m , and local relief exceeding 0.8 km/km . In our investigation, we did not focus on any specific landslide, or group of landslides. Instead, we exploited the new geomorphological inventory of landslides in VM to determine the statistics of landslide area A_L and volume V_L , and the Heims' ratio H_L/L_L for the mapped Martian landslides, and to discuss similarities and differences with similar statistics obtained for terrestrial landslides. To investigate the possible triggers of the very large landslides ($A_L > 10^8 \text{ m}^2$) in VM, we adopted a rigorous Limit Equilibrium Method (LEM) (Duncan, 1996; Krahn, 2003; Zhu et al., 2005; Borselli, 2013) and we performed slope stability analyses for a selected set of failures. Results indicate that seismic shaking caused e.g., by impact events, faulting, or volcanic activity, is the probable cause for the very large Martian landslides.

2. Landslide identification, mapping, and classification

When single or multiple landslides occur in an area, they change local topography and radiometric properties of the land surface, leaving discernible morphometric (Pike, 1988) and radiometric (Guzzetti et al., 2012) signatures that can be detected and interpreted. To detect and map landslides and other mass wasting features in Tithonium and Ius Chasmata, VM, we analysed visually the optical images acquired by the High-Resolution Stereo Camera (HRSC, Neukum et al., 2004; Jaumann et al., 2007) on board the Mars Express spacecraft, and by the Context Camera (CTX, Malin et al., 2007) on board the Mars Reconnaissance Orbiter (MRO). The HRSC and CTX images have a ground sampling distance (GSD) of $\sim 15 \text{ m/pixel}$ and $\sim 6 \text{ m/pixel}$, respectively. Although examples exist of the use of THEMIS IR images for landslide mapping (Lucas et al., 2011), we maintain that the resolutions provided by the HRSC and CTX images are better suited to detect and map landslides on Mars with unprecedented details and geographical accuracy. In addition, we analysed the local topography using the elevation information obtained at 463 m/pixel resolution by the Mars Orbiter Laser Altimeter (MOLA, Zuber et al., 1992) on board the Mars Global Surveyor (MGS) spacecraft. We exploited the MOLA digital elevation model (DEM) to reconstruct 3D views of the landslide areas, to facilitate mapping of individual slope failures and their internal features, and to evaluate the volume of some of the mapped landslides.

To recognise and map landslides and other mass wasting features in VM, we adopted the same visual criteria commonly used by geomorphologists to recognise terrestrial landslides in large areas through the interpretation of aerial photographs or satellite images of similar characteristics, including shape, size, tone, mottling, texture, pattern of objects, site topography, and setting (Antonini et al., 2002; Guzzetti et al., 2012). Slope failures were classified according to Cruden and Varnes (1996), based on the morphological similarity with terrestrial landslides. No specific inference was made on the geomorphological setting or the processes that may have triggered, or modified locally, the Martian slope failures.

In Tithonium and Ius Chasmata, we recognised and classified the following five types of mass movements: (i) slides (RS), including rock slides and deep-seated slides, (ii) complex/compound slides (CL), (iii) rock avalanches (RA), (iv) debris flows (DF), including debris avalanches and shallow debris slides, and (v) rock glacier-like features (RG). Fig. 1 shows representative examples of the five types of mass movements, together with examples of terrestrial analogues (larger images are given in the Supplementary material for improved readability). Fig. 2a shows the complete geomorphological landslide inventory map for our study area

(additional examples of the mapped landslides are in the Supplementary material), and Table 1 lists descriptive statistics for the mapped mass movements. For two sites in the study area (b and c/d white boxes in Fig. 2a) we recognised and mapped additional geomorphological features related to the presence of mass wasting processes, including talus deposits, rock cliffs and associated escarpments, and the surface traces of trenches on the flat uplands bounding the VM (Figs. 2b, c and d).

We here describe the five types of geomorphological features that have allowed us to classify the different types of mass movements in VM (Fig. 1). Rock slides (RS) and complex/compound slides (CL) exhibit kilometre-scale (2 to 3 km in height) escarpments that originate consistently from the top of the chasmata (Fig. 2a). This is the evidence that deep-seated landslides have sculptured the walls of the chasmata, and have contributed to the widening of the canyons. The escarpments of the RS are curved and slightly concave upward, indicating a (at least partial) rotational movement of the material in the landslide depletion area. This provides information on the shape of the failure planes, and on the kinematics of the slope failures. The deposits of the RS are characterised by an irregular and hummocky topography (Fig. 1a). This is typical of large terrestrial rock slides. In places, some of the large deposits are affected by partial reactivations (see Figs. 7.S and 8.S in the Supplementary material). Based on these morphological characteristics, we consider that the Vajont rock slide of 9 October 1963 (Fig. 1b), Italy, is a good terrestrial analogue of the RS identified and mapped in VM. In comparison to the RS, the deposits of the complex/compound slides (CL) in VM exhibit a smoother and more regular topography (Fig. 1c). Complex landslides (CL) involve both sliding and flowage, and they show a structured deposit and debris aprons with longitudinal ridges and minor scarps produced by differential movements within the displaced material (Cruden and Varnes, 1996). The deposits of the CL are characterised by single, or by sets of trenches and ridges that align parallel and/or orthogonally to the local direction of motion of the landslide material. This is indicative of a rapid- to fast-moving flow mechanism for the emplacement of the failed materials (Pierson and Costa, 1987). Where the bottom of the chasmata is large, individual CL deposits have travelled for tens of kilometres (Quantin et al., 2004a), suggesting a high mobility of the failed materials. We take the Bairaman River landslide, Papua New Guinea (Fig. 1d), as a terrestrial analogue for the CL identified in VM. In our study area, the failures mapped as rock avalanches (RA) are characterised by very steep slopes in the source and transport areas, with large and flat depositional zones at the bottom of the slopes and in the flat valley bottoms (Fig. 1e). The landslide deposits exhibit a rough topographic surface, which we consider to be a consequence of coarseness of the materials in the deposits. The Mount Cook rock avalanche, New Zealand (Fig. 1f), is a terrestrial analogue for the RA in the VM. In our classification, debris flows, debris avalanches, and shallow debris slides in the VM, collectively mapped as DF, are significantly smaller in area and volume with respect to the slides (RS, CL) and the rock avalanches (RA) present in the same area. The shallow slope failures exhibit a relatively small and surficial escarpment, a channel-shaped depletion/transport zone, and a distinct and fan-shaped depositional zone (Fig. 1g). Close visual inspection of high resolution CTX images revealed a texture in the depositional zones (or portions of them) characterised by different roughness of the topographic surface. This is indicative of the presence of materials of different grain sizes in the debris deposits, or in different parts of the DF deposits. This is a typical feature of terrestrial debris flows. As a terrestrial analogue for the DF in VM we have selected the Slocbhaig debris flow, Scotland (Fig. 1h). Furthermore, in the study area we observed rock glacier-like features (RG). These elongated features are characterised by shallow deposits with distinct lateral levees and single or multiple, linear

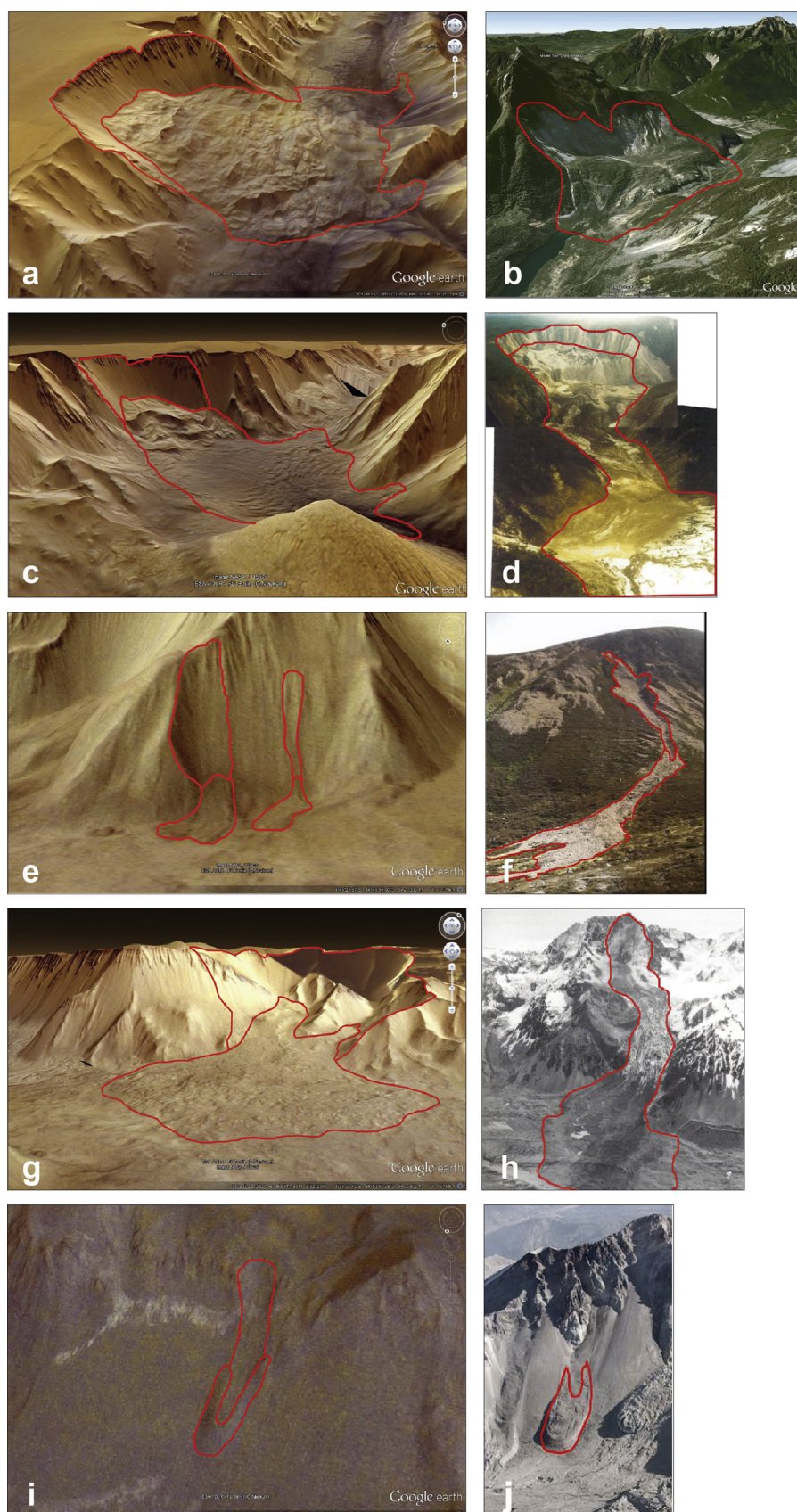


Fig. 1. Comparison of mass wasting features detected and mapped in Valles Marineris, Mars (source: Google Mars™), with terrestrial analogous. (a) Rock slide (RS), and (b) Vajont rock slide, Mount Toc, Italy (source: Google Earth™); (c) complex/compound landslide (CL), and (d) Bairaman River landslide, Papua New Guinea (source: Landslides of the World, edited by K. Sassa, 1999); (e) debris flow (DF), and (f) Slocach Bheag debris flow, Ben Avon, Scotland (source: www.landforms.eu/cairngorms/debris_flow.htm); (g) rock avalanche (RA), and (h) Mount Cook rock avalanche, New Zealand (source: Landslides of the World, edited by K. Sassa, 1999); (i) rock glacier-like feature (RG), and (j) Mount Saint Helens rock glacier, Washington, USA (source: rockglacier.blogspot.com/2010/05/mount-st-helens-30-years-of.html).

Table 1

Descriptive statistics for mass wasting features mapped in the 10^5 km^2 study area in Tithonium and Ius Chasmata, Valles Marineris, Mars.

Feature type	Count (#)	A_{MIN} (km^2)	A_{MAX} (km^2)	A_{AVG} (km^2)	A_{TOT} (km^2)	
DF	Debris flow	89	0.3	0.7×10^3	3.2×10^1	2.8×10^3
RS	Rock slide	50	0.5	4.4×10^3	3.4×10^2	1.7×10^4
CL	Complex/Compound landslide	33	1.3	8.7×10^3	0.8×10^3	2.5×10^4
RA	Rock avalanche	26	3.6	0.8×10^3	0.8×10^2	1.9×10^3
RG	Rock glacier like	21	0.5	1.5×10^1	0.5×10^1	1.1×10^2
All mapped features		0.3	8.7×10^3	2.1×10^2	4.4×10^4	

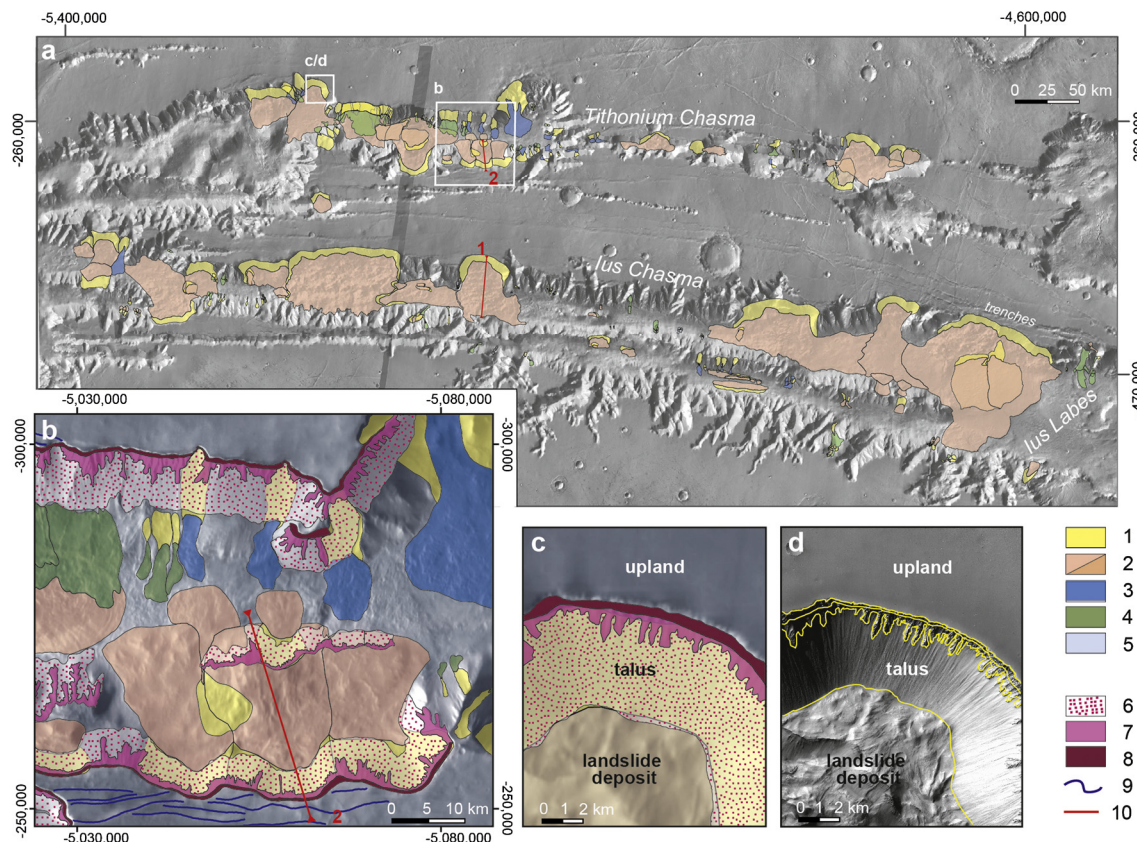


Fig. 2. Geomorphological landslide inventory map for the Tithonium and Ius Chasmata region, Valles Marineris, Mars. (a) The study area at $\approx 1:5,000,000$ scale. (b) Details of a portion of the inventory in Tithonium Chasma at $\approx 1:43,000$ scale. (c) Enlargement of a landslide source area. Background for (a), (b) and (c) is a THEMIS infrared Global Mosaic (100 m/pixel) draped on the MOLA DEM (Christensen et al., 2004). (d) Portion of CTX image for the same area shown in (c). Colours of the mapped units show landslides of different types, and relative ages. Legend: (1) landslide scarp (source area). (2) Deposit of slide, including rock slides (RS), complex and compound failures (CL). Relative age shown by different shades of colour, from older (light) to younger (darker). (3) Deposit of rock avalanche (RA). (4) Debris flow (DF), including debris avalanches and shallow debris slides. (5) Rock glacier-like features (RG). (6) Talus. (7) Bedrock. (8) Rock cliff. (9) Surface trace of trench. (10) Position of profiles used in slope stability analysis (see Fig. 8). (For interpretation of the references to color in this figure, the reader is referred to the web version of this article.)

or sinuous ridges, with a typical topographic signature (Fig. 1i) similar to the characteristics of terrestrial rock glaciers, including the Mount Saint Helens rock glacier, USA, shown in Fig. 1j.

Overall, in our study area we mapped a total of 219 mass wasting features, including 198 landslides (RS, CL, RA, DF) and 21 rock-glaciers-like (RG) features (Table 1). The mapped mass movements are in the range $0.3 \text{ km}^2 < A_L < 8.7 \times 10^3 \text{ km}^2$, for a total surface $A_{\text{LT}} = 4.4 \times 10^4 \text{ km}^2$, occupying 44% of the study area (10^5 km^2). This is a larger number of failures than previously recognised in the same general area (Quantin et al., 2004a). Based on the resolution and quality of the HRSC and the CTX images used to recognise and map the landslides, and on our experience of mapping terrestrial landslides using conventional aerial photography and modern satellite imagery (Guzzetti et al., 2012), we consider that the new geomorphological landslide inventory is statistically complete for landslides with $A_L > 1.5 \times 10^6 \text{ m}^2$ (189 landslides). We attribute the improved mapping accuracy of the new geomorphological in-

ventory for VM to the high spatial resolutions of the HRSC and CTX images used to map the landslides, and to the systematic approach adopted for their identification and mapping (Guzzetti et al., 2012).

In places, the visual interpretation of the satellite images allowed mapping multiple generations of slope failures, i.e., younger landslides nested inside older (pre-existing) failures (Figs. 3a and 3b). Although the age and the temporal relationships of the landslides of different ages remain undermined, we consider the finding indicative of multiple landslide triggering events, or of local internal adjustments (reactivations) of portions of the larger landslide deposits to reach more stable conditions. All the mapped landslides originated from the walls of the chasmata, and not from the interior layered deposits (ILDs) that are widespread in the canyon floors of the VM (e.g., Nedell et al., 1987; Komatsu et al., 1993). Mass wasting features originating from the ILDs were iden-

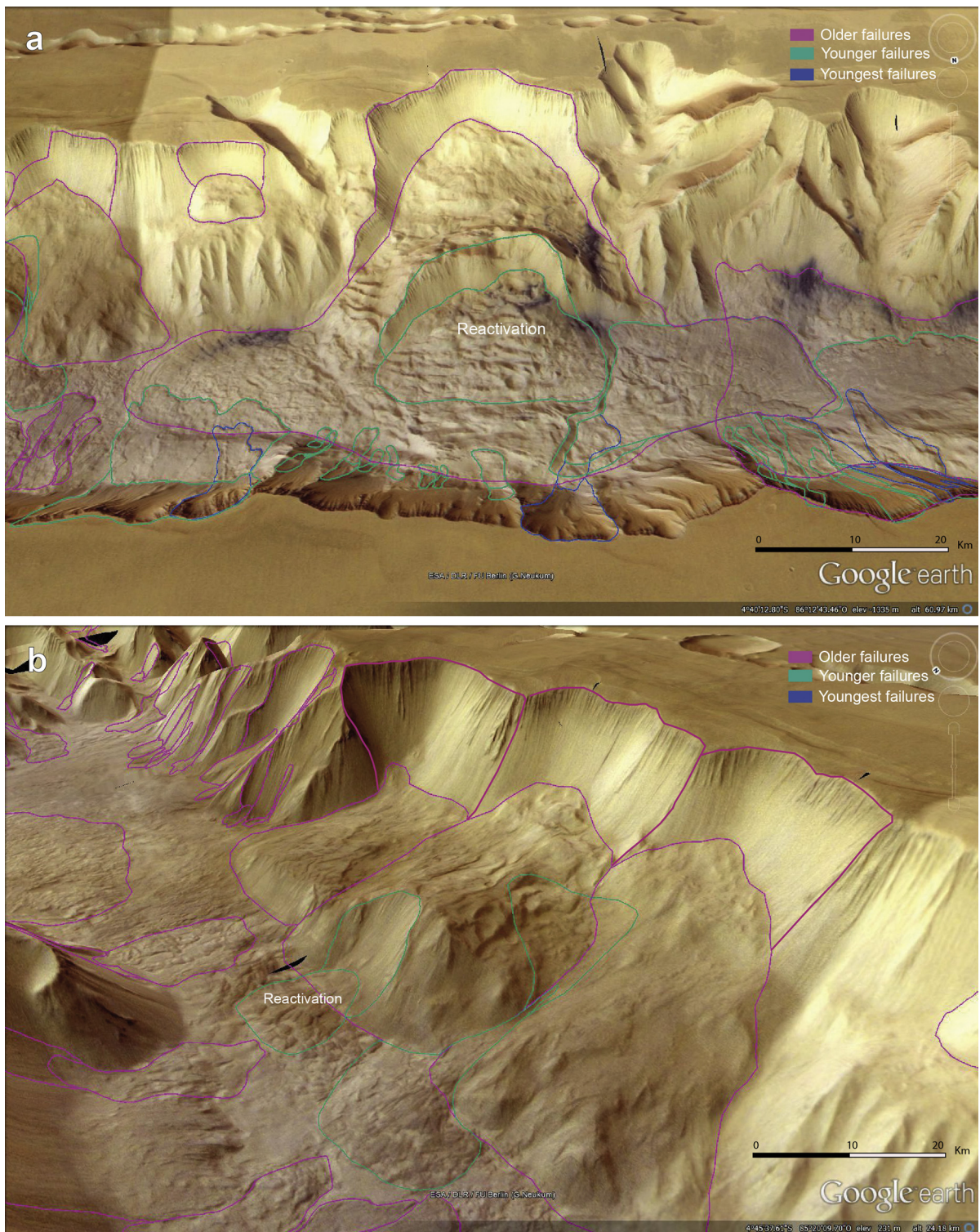


Fig. 3. (a) and (b) Maps showing multiple generations of slope failures in a portion of the study area. Purple contours are failures older than the green (younger) and the blue (youngest) landslides. Background shows HRSC mosaic (~ 15 m/pixel) draped on MOLA DEM (Christensen et al., 2004). (For interpretation of the references to color in this figure, the reader is referred to the web version of this article.)

tified in other regions of the VM (e.g., Neuffer and Schultz, 2006), but not in our study area.

Landslides in the two chasmata have local terrain gradients computed from the MOLA DEM in the range between 0° and 45° , with a mean value $\mu = 11^\circ$ (standard deviation, $\sigma = 9^\circ$). In the same region, the stable slopes (i.e., the slopes that have not failed) exhibit terrain gradients in the range from 0° to 63° , with a significantly larger mean value $\mu = 21^\circ$ ($\sigma = 7^\circ$). This is evidence that

the mass movements have reduced the slopes of the chasmata by $\sim 10^\circ$, a considerably larger value than that observed on Earth (e.g., Guzzetti et al., 2008).

3. Statistics of landslide size

We measured the planimetric area A_L of 198 landslides of the RS, CL, RA and DF types. For a subset of 49 landslides, we have also

estimated the volume V_L of the deposits of the individual failures. For 51 RS and CL whose run out was not constrained by topographic obstacles (e.g., a wall of the chasma), we measured the run-out length L_L and the fall height H_L , and determined the mobility index H_L/L_L (Legros, 2002), also known as Heim's ratio (Hsü, 1975; Davies, 1982; Dade and Huppert, 1998), and equivalent to the apparent friction angle of Scheidegger (1973). We used the geometric measurements to: (i) establish the probability density of landslide area $p(A_L)$ and landslide volume $p(V_L)$, (ii) determine an empirical relationship to link the area and volume of the Martian landslides, and (iii) compare the obtained statistics and empirical relationship for the Martian landslides to similar statistics and relationships available for terrestrial landslides (Legros, 2002; Imre, 2004; Malamud et al., 2004; Bigot-Cormier and Montgomery, 2007; Guzzetti et al., 2009; Larsen et al., 2010).

For each landslide, the planimetric area A_L was obtained in a Geographic Information System (GIS). Given the complexity of the morphology of the landslide terrain (see examples in the Supplementary material), the local presence of multiple generations of slope failures (e.g., Figs. 7.S and 8.S in the Supplementary material), and the quality and resolution of the images used to detect and map the landslides, we estimate that the error in the geometric measurement of the landslide area is $\varepsilon_A = \pm 0.2 \times A_L$, i.e., 20% of A_L . The estimated 20% relative error in the measurement of the landslide area is obtained from the worst resolution of the images used to map the landslides (HRSC ~ 15 m/pixel). For each landslide, we calculated the maximum relative error (in percentage) by multiplying the landslide perimeter with the width of a pixel (15 m for HRSC), and dividing the result by the landslide area. For the landslide dataset we calculated a maximum value of 18%.

For 49 landslides we determined the volume of the landslide deposit, V_L . Due to fragmentation, the volume of the landslide deposit is larger than the volume of the failed mass, i.e., the volume of the bedrock materials before failure. However, we maintain that the difference is not relevant for our investigation. Further, statistics of landslide volume (Malamud et al., 2004; Brunetti et al., 2009) and empirical relationships linking A_L to V_L (Guzzetti et al., 2009; Larsen et al., 2010) are determined typically measuring or estimating the volume of landslide deposits. To estimate V_L , we reconstructed the three-dimensional (3D) geometry of the landslide failure plane in the GIS. For the purpose, we obtained 3D coordinates (latitude, longitude, elevation) of points equally spaced along the boundary of the mapped landslide deposit, and we used this geometrical information to reconstruct the geometry of the failure plane. To account for the uncertainty associated with the identification of the failure plane, we selected a deeper and a shallower surface, bracketing the range of plausible failure planes, based on local topographical and geomorphological constraints. In the GIS, we then computed the volumetric difference between the topographic surface and the shallower (minimum volume) and the deeper (maximum volume) surfaces. The two volumetric estimates were averaged to obtain the volume of the landslide used in the study, V_L . Considering the morphological complexity of the landslides, the quality and resolution of the DEM used to calculate V_L , the uncertainty associated to the definition of the landslide volume, and the differences between the minimum and the maximum volumes computed for each failure, we estimated a maximum error of a factor of two in the geometric estimation of the landslide volume (Brunetti et al., 2009). In other words, the real volume of a landslide can be a half ($0.5 \times V_L$) or twice ($2 \times V_L$) the estimated volume. The uncertainty in the estimation of V_L is therefore $(\varepsilon_V)_- = -0.5 \times V_L$ and $(\varepsilon_V)_+ = +2 \times V_L$. This estimated error is sufficiently large to include the volumetric differences obtained considering different possible geometries for the landslide source area, or detachment zone (e.g., 128% in Lucas et al., 2011).

Linear measurements of the landslide run-out L_L and the landslide fall height H_L were obtained using the landslide profile projection available in Google Mars™. For the length measurements, we have estimated maximum relative errors of $\varepsilon_L = 0.1 \times L_L$ and $\varepsilon_H = 0.1 \times H_L$, i.e., 10% of L_L and H_L , respectively.

3.1. Landslide area

On Earth, the non-cumulative probability density of landslide area $p(A_L)$, exhibits a typical shape, with the abundance of landslides increasing with their size up to a maximum value (rollover), after which the number of landslides decreases rapidly following a power law with scaling exponent α (Stark and Hovius, 2001; Guzzetti et al., 2002; Malamud et al., 2004; Van Den Eeckhaut et al., 2007). We determined two non-cumulative probability densities of the landslide area $p(A_L)$ for the 82 RS and CL, and for the 198 landslides of all types (RS, CL, RA, DF) mapped in VM. For the purpose, we used kernel density estimation (KDE, Silverman, 1986; Venables and Ripley, 2002). In an attempt to consider the uncertainty associated with the empirical measurements of A_L ($\varepsilon_A = \pm 0.2 \times A_L$), we adopted a random extraction approach to calculate $p(A_L)$. First, the empirical A_L data were log-transformed to account for problems associated with the fitting of data spanning multiple orders of magnitude. Next, we constructed 5000 synthetic data sets, each set having the same number of data values ($n = 82$), with each synthetic value obtained by sampling randomly from a uniform distribution bounded by the relative measurement error $[A_L - \varepsilon_A, A_L + \varepsilon_A]$. Finally, the 5000 synthetic data sets were used to obtain the mean μ and the standard deviation σ of the scaling exponent α that measures the slope of the tail of the distribution for the large and very large landslides.

Figs. 4a and 4b show the $p(A_L)$ for the 82 slides of the RS and the CL types, and for the 198 landslides of all types, respectively. In both figures, red dots show landslides that were not constrained by the local topographic setting, and yellow dots show landslides constrained by the local topographic setting (e.g., the opposite slope of the chasmata). The red line is a power law fit of the $p(A_L)$ for landslides not constrained by topographic obstacles (red dots). Figs. 4a and 4b also show the $p(A_L)$ for 4233 shallow and deep-seated landslides, mostly of the slide and complex types, caused by rapid snow melting in Umbria, Italy, in January 1997 (Cardinali et al., 2000; Malamud et al., 2004), and for 894 deep-seated historical landslides, also of the slide and complex types, mapped by Cardinali et al. (1990) in New Mexico, USA. The probability density function $p(A_L)$ for shallow and deep-seated landslides in Umbria are modelled by the inverse Gamma distribution (purple line) proposed by Malamud et al. (2004).

The non-cumulative probability density $p(A_L)$ of the RS and CL in VM follows a power law trend for most of the range of the mapped landslides ($5 \times 10^5 \text{ m}^2 < A_L < 10^{10} \text{ m}^2$), with a scaling exponent of the distribution $\alpha = -1.01 \pm 0.01$, considerably smaller (heavier tail) than the scaling observed for the terrestrial slides ($\alpha = -2.2$ and -2.4) (Malamud et al., 2004). Including all types of landslides in VM, the scaling exponent is slightly larger ($\alpha = -1.35 \pm 0.01$), but remains significantly lower than the exponents found for the terrestrial slides and for landslides of other types (Van Den Eeckhaut et al., 2007). As a consequence, the proportion of very large (i.e., $A_L > 10^7 \text{ m}^2$) landslides is larger on Mars than on Earth. Deviation from the power law trend for landslides with $A_L > 10^8 \text{ m}^2$ (yellow dots in Figs. 4a and 4b) is due to local topographic conditions that limited the further expansion of the failures. The effect of local topography in the determination of the maximum size of landslides was observed also for very large terrestrial landslides (Guzzetti et al., 2002).

Recently, Crosta et al. (2013) have presented an analysis of the areas of 1232 landslides in the entire VM. The non-cumulative

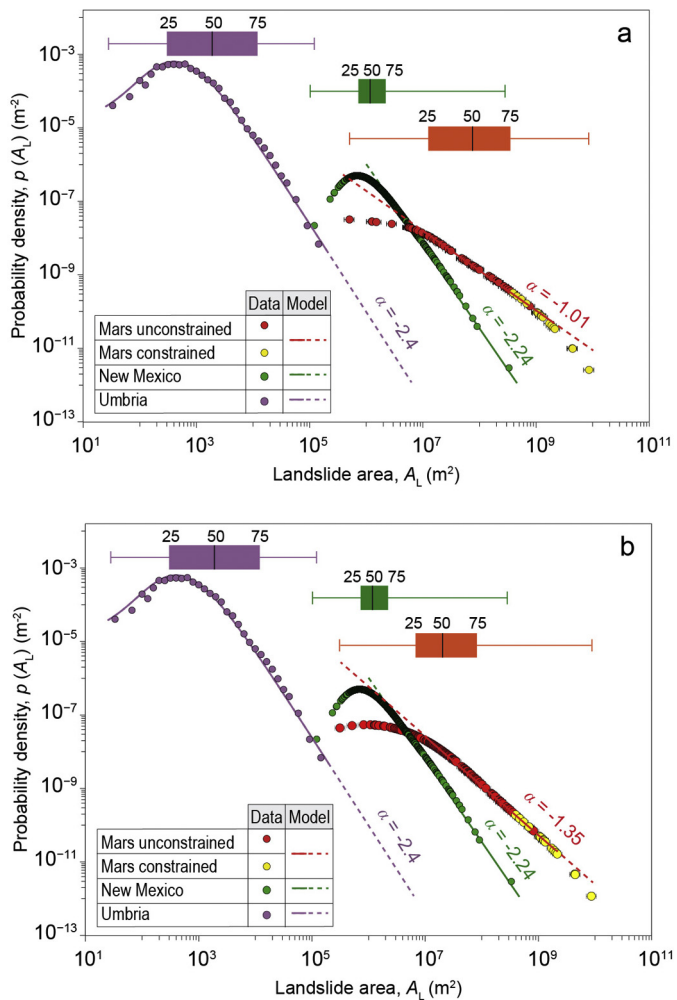


Fig. 4. Statistics of landslide areas for landslides mapped in Tithonium and Ius Chasma, Valles Marineris, Mars. (a) Non-cumulative probability density of landslide area $p(A_L)$ for 82 Martian slides (red dots for landslides not constrained by local topographic setting, yellow dots for landslides constrained by local topographic setting); 4233 snowmelt-induced event landslides in Umbria, Italy (Cardinali et al., 2000; Malamud et al., 2004) (violet dots); and 894 historical landslides in New Mexico (Cardinali et al., 1990) (green dots). Colour lines show corresponding best fit models. Box plots show statistics of A_L . (b) Same as (a) for the entire dataset (198) of landslides mapped in the study area. (For interpretation of the references to color in this figure, the reader is referred to the web version of this article.)

probability density $p(A_L)$ for their dataset followed a power law with a gentler scaling exponent $\alpha = -1.11$ for $1 \times 10^9 \text{ m}^2 < A_L < 5 \times 10^{11} \text{ m}^2$, and a steeper power law with $\alpha = -2.19$ for $6 \times 10^{11} \text{ m}^2 < A_L < 2 \times 10^{13} \text{ m}^2$. In the range of A_L covered by our inventory, the scaling exponent of the $p(A_L)$ matches the exponent found by Crosta et al. (2013).

3.2. Landslide volume

On Earth, the volume of the deposit of single subaerial landslides spans the range of $10^{-4} \text{ m}^3 < V_L < 10^{11} \text{ m}^3$ (Brunetti et al., 2009; Guzzetti et al., 2012). The subset of 49 landslides in our inventory for which we estimated the volume of the deposit is in the range of $10^7 \text{ m}^3 < V_L < 10^{12} \text{ m}^3$, confirming that individual Martian landslides are larger than corresponding terrestrial failures, and are in the range of the largest submarine terrestrial slope failures (Locat and Lee, 2009; Ten Brink et al., 2006). However, the deposits of the deep-seated slides in VM exhibit an average terrain gradient $\mu = 7.8^\circ$ ($\sigma = 5.9^\circ$) significantly larger than the average terrain gradient of submarine terrestrial landslides ($\mu < 3^\circ$). Based

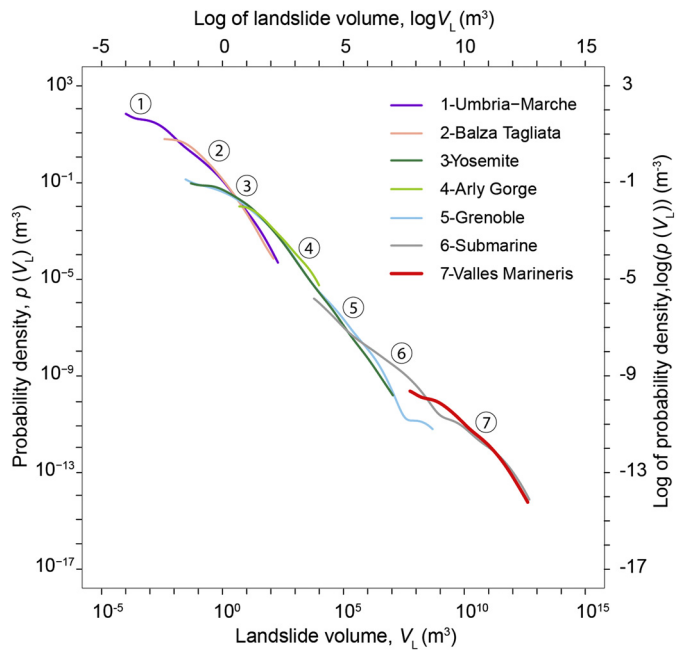


Fig. 5. Statistics for landslide volumes for landslides mapped in Tithonium and Ius Chasma, Valles Marineris, Mars. Comparison of non-cumulative probability density of landslide volume $p(V_L)$ for 49 slides in the VM (red curve) and for terrestrial data sets of terrestrial, sub aerial rock falls and rock slides (Brunetti et al., 2009). Non-cumulative probability density of submarine landslides is also shown (grey curve). (For interpretation of the references to color in this figure, the reader is referred to the web version of this article.)

on this observation, we hypothesise that the deep-seated slides in VM formed in sub aerial conditions.

On Earth, the non-cumulative probability density of the volume of landslides of very different sizes ($10^{-4} \text{ m}^3 < V_L < 10^{11} \text{ m}^3$) obeys a power law distribution for landslide volumes exceeding a minimum threshold, with a scaling exponent that depends on the type of the failure (Brunetti et al., 2009). To determine the probability density of the volume of the VM landslides $p(V_L)$, we adopted the same procedure used to estimate $p(A_L)$ (see Section 3.1). A random extraction was applied to evaluate the mean value and the uncertainty associated with the scaling exponent of the probability density of the landslide volume $p(V_L)$. Our data set of 49 deep-seated slides in VM (Fig. 5) obeys a negative power law trend in the range $10^9 \text{ m}^3 < V_L < 10^{12} \text{ m}^3$, with a scaling exponent $\beta = -1.03 \pm 0.01$. This value is typical of terrestrial failures dominated by a brittle behaviour, i.e., rock falls and rock slides (Brunetti et al., 2009). This evidence is consistent with the predominant type of landslides the mapped in the VM, i.e., rock slides (RS) (Fig. 1a).

3.3. Relationship between landslide area and volume

A combined analysis of the measurements of A_L and V_L for a subset of 49 deep-seated slides in VM allowed determining an empirical relationship linking the area to the volume of the Martian landslides. To determine the dependency, we adopted a power law equation of the form $V_L = \eta \times A_L^\gamma$, which was fitted to the empirical data using robust linear fitting to minimise the effects of possible outliers (Venables and Ripley, 2002). The obtained empirical relationship is $V_L = (1.2 \pm 0.8) \times A_L^{(1.25 \pm 0.03)}$, which is directly comparable to similar equations obtained for terrestrial landslides. In particular, Guzzetti et al. (2009) found $V_L = 0.074 \times A_L^{(1.450 \pm 0.009)}$ for 677 terrestrial landslides predominantly of the slide type. Larsen et al. (2010) obtained $V_L = 0.146 \times A_L^{(1.332 \pm 0.005)}$ for 4231 landslides of all types, and $V_L = 0.186 \times A_L^{(1.35 \pm 0.01)}$ for a subset

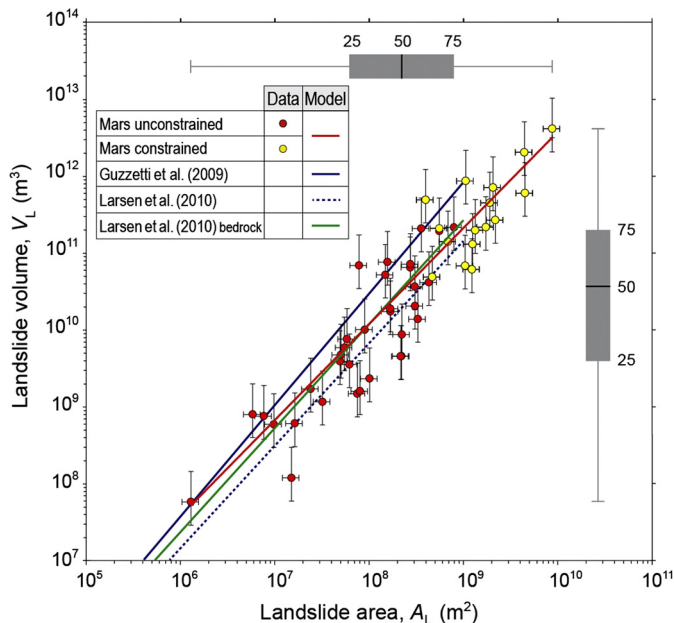


Fig. 6. Dependence of landslide volume V_L on landslide area A_L for 49 landslides mapped in Tithonium and Ius Chasmata, Valles Marineris, Mars. Red dots show unconstrained landslides and yellow dots show landslides constrained by local topographic setting. Red line shows equation $V_L = 1.2 \times A_L^{1.25}$ obtained through robust linear fitting. Solid and dashed blue lines, and green lines are similar relationships for terrestrial landslides (Guzzetti et al., 2009; Larsen et al., 2010). Box plots show statistics of A_L (right) and V_L (top) for landslides in the VM. (For interpretation of the references to color in this figure, the reader is referred to the web version of this article.)

of 604 bedrock landslides. Fig. 6 compares the relationship obtained for the landslides in the VM (red) with the relationships obtained by Guzzetti et al. (2009) for slides (blue), and by Larsen et al. (2010) for all landslide types (dotted blue), and for bedrock landslides (green). The visual comparison reveals that the relationship for the Martian landslides is similar to the distribution found on Earth for bedrock landslides. This is not surprising, because the subset of Martian landslides used to construct the dependency comprises deep-seated landslides that involve the bedrock (see Figs. 2b and 2c).

We used the new empirical relationship to estimate the volume of all the 83 landslides (RS, CL) mapped in VM from their planimetric area. Results indicate that the total volume of landslide material in the study area is $V_{LT} = 1.3_{-1.1}^{+3.1} \times 10^{13} \text{ m}^3$. This is equivalent to an average thickness of landslide material ranging from 23 m to 450 m. The result compares to (i) an average value of 5.7 obtained for the 4098-km² Upper Tiber River catchment, in central Italy (Guzzetti et al., 2008), and (ii) an average value of 2.7 m obtained for a 79-km² hilly area also in central Italy (Guzzetti et al., 2009), and it is consistent with the higher average thickness of landslides on Mars.

3.4. Landslide mobility

We measured the run-out length L_L and the fall height H_L of 83 slope failures of the RS, CL, RA, and DF types in the VM (Table 1.S in the Supplementary material). We selected failures whose run out was not affected by local topographic constraints e.g., the presence of the opposite slope of the chasma. In the absence of forces other than Coulomb friction and gravity, the H_L/L_L ratio, known also as Heim's ratio, which is equivalent to the tangent of the apparent friction angle ϕ (Scheidegger, 1973; Hsü, 1975), and to the inverse of the overall mobility of the

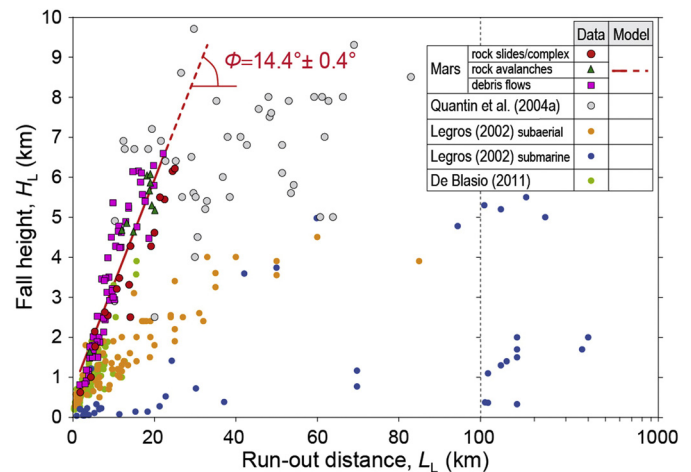


Fig. 7. Dependence of landslide fall height H_L on run out distance L_L for 51 unconstrained landslides mapped in Tithonium and Ius Chasmata, Valles Marineris, Mars (this study), and for previously published Martian (Quantin et al., 2004a) and terrestrial (subaerial and submarine) failures (Legros, 2002; De Blasio, 2011). Red line shows the relationship $H_L = 0.29 \times L_L$ obtained through linear fitting. (For interpretation of the references to color in this figure, the reader is referred to the web version of this article.)

failed mass (Davies, 1982; Dade and Huppert, 1998; Legros, 2002; Imre, 2004; Bigot-Cormier and Montgomery, 2007). The H_L/L_L ratio is different from the effective friction of the materials involved in the failure, which can be determined through modelling (Lucas and Mangeney, 2007).

Fig. 7 shows the empirical data subdivided by landslide type (red dots are RS and CL, green triangles are RA, purple squares are DF). Our measurements are well approximated by a linear fit corresponding to an apparent friction angle $\phi = 14.4^\circ \pm 0.4^\circ$. The calculated value, and the associated uncertainty, was obtained from 10 000 synthetic series of H_L and L_L of the same length of the original series ($n = 83$). Each synthetic value of H_L^* was obtained through random sampling from a uniform distribution centred around the measured values H_L , and with a range corresponding to the assumed measurement uncertainty of 10%, $[0.9H_L, 1.1H_L]$. The same was performed for L_L . For comparison, in Fig. 7 we show the H_L and L_L measurements for 82 subaerial and 44 submarine landslides (Legros, 2002), 91 subaerial landslides (De Blasio, 2011), and measurements for 45 landslides in VM mapped by Quantin et al. (2004a).

The resulting apparent friction angle is comparable to previous estimates obtained for landslides in VM. For example, Schultz (2002) back-calculated the stability of slopes in VM with the method of slices, and obtained friction angles in the range $14^\circ < \phi < 25^\circ$ for the stronger wall rock (bedrock), and in the range $5^\circ < \phi < 18^\circ$ for the weaker interior deposits. Imre (2004) used a distinct element code applied to wall rocks in the Candor Chasma, approximately 800 km to the E of our study area, to determine $\phi = 22^\circ \pm 2^\circ$. Bigot-Cormier and Montgomery (2007) used the Culmann wedge model to predict the maximum stable height and the apparent friction angle $8^\circ < \phi < 10^\circ$ for 36 landslides in VM. Using data on friction coefficients for 45 landslides reported in Table 1 of Quantin et al. (2004a), we calculated for their data set an apparent friction angle $\phi = 12^\circ \pm 7^\circ$.

4. Slope stability analysis

We performed Limit Equilibrium Method (LEM, Duncan, 1996; Krahn, 2003; Chowdhury et al., 2009) slope stability analyses along two reconstructed topographic profiles on the opposite slopes of the central parts of Tithonium and Ius Chasmata (red lines in the maps of Fig. 8). The topographic profiles were reconstructed

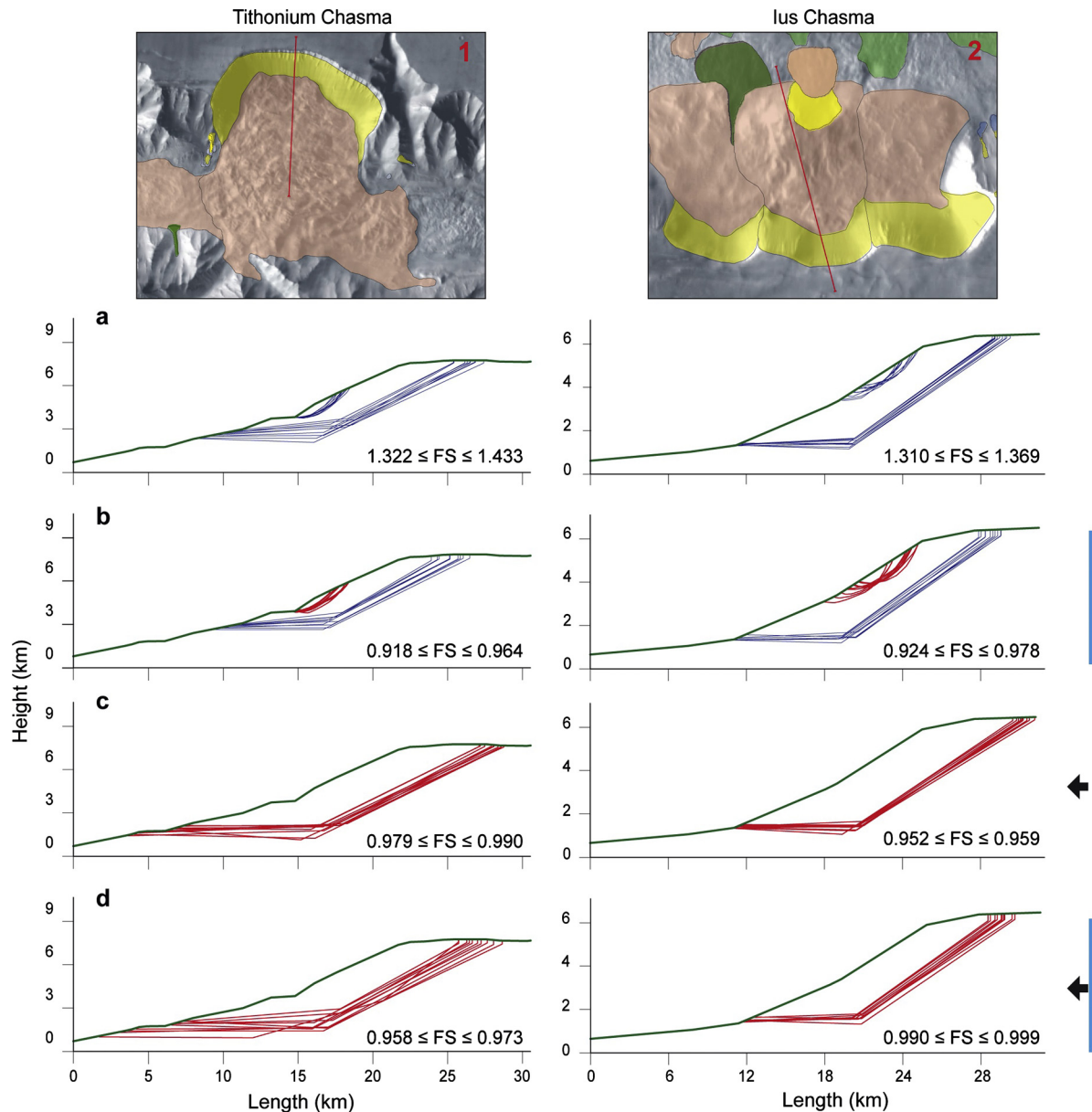


Fig. 8. Results of slope stability analyses performed along two representative slopes in Tithonium Chasma (left charts) and Ius Chasma (right charts). (a) Dry slope and no external forcing. (b) Fully saturated slope (vertical blue bar) and no external forcing. (c) Dry slope and external seismic forcing (black arrow). (d) Fully saturated slope and external seismic forcing (vertical blue bar and black arrow). Each chart shows ten sliding surfaces with the smallest computed Factor of Safety (FS) obtained adopting a Limit Equilibrium Method approach. Blue lines show sliding surfaces with $FS > 1$ (stable conditions). Red lines show sliding surfaces with $FS \leq 1$ (unstable conditions). Green lines show topographic profiles. (For interpretation of the references to color in this figure, the reader is referred to the web version of this article.)

Table 2

Geo-mechanical parameters used for the slope stability calculations in Tithonium and Ius Chasmata, Valles Marineris, Mars.

Parameter	Unit	Value
Surface gravity	$m s^{-2}$	3.7
Rock unit weight	$kN m^{-3}$	10.7
Water unit weight	$kN m^{-3}$	3.7
Water saturated rock unit weight	$kN m^{-3}$	11.1
Uniaxial compressive strength of intact rock*	MPa	90
Horizontal pseudo-static seismic coefficient, K_h	–	0.19–0.31
Geological Strength Index, GSI*	–	30–70
m_i value for basalt rock mass*	–	25
Disturbance factor, D^*	–	1.0

* Parameters related to rock mass strength criteria (Hoek et al., 2002).

considering the morphology of the landslides and of the stable slopes to the side of the failed slopes (see also red lines 1 and 2 in Fig. 2a). Each profile covers about 30 km, with a mean slope

in the range 25° – 30° , and is representative of the topographic and morphological conditions prior to failure. For slope stability modelling we used the Slope Stability Analysis Program code, SSAP2010, version 4.0.8 (<http://www.ssap.eu>, Borselli 2013, 2014), adopting a LEM that exploited the Morgenstern–Price rigorous approach (Zhu et al., 2005). To identify the sliding surfaces with the minimum stability conditions, we exploited generalised computational and searching strategies (Boutrup and Lovell, 1980; Siegel et al., 1981) using a Monte Carlo method and pattern search. We considered different geometries for the potential sliding surfaces, and we determined the depth of the tension crack in the landslide detachment zone automatically, considering where the horizontal inter-slice force was negative due to the prevalence of traction forces (Chowdhury et al., 2009). For modelling purposes, we hypothesised that the landslides were the product of a single failure event. This is entirely consistent with the internal morphological

appearance of the modelled landslides, the landslide geometry, and the local structure. The mechanical properties used for modelling are listed in Table 2. To determine equivalent shear strength Mohr-Coulomb parameters for the rock mass along the potential sliding surfaces, we adopted a parameterisation of the mechanical properties based on the dimensionless Geological Strength Index (GSI) in the range 30–70, a constant value for the coefficient $m_i = 25$ (typical of a basalt, Schultz (2002), Bigot-Cormier and Montgomery (2007)), and a constant disturbance factor $D = 1.0$ (Hoek et al., 2002). Borselli et al. (2011) have performed a similar analysis to investigate the general stability conditions of the Volcán de Colima, Mexico. Results of the modelling in VM constrained realistic GSI values in the range 40–50, characteristic of a medium quality rock mass. Seismic effects were considered in the analysis, adopting a pseudo-static approach (Ashford and Sitar, 2002) in which the horizontal and the vertical seismic coefficients, K_h and K_v , depend on the maximum peak ground acceleration (PGA) (Sarma, 1973; Makdisi and Seed, 1978; Chowdhury et al., 2009), and account for the increase in the vertical and the horizontal components of the inertial force.

We tested four possible stability conditions, including: (a) a dry slope, (b) a fully saturated slope, (c) a dry slope with seismic forcing, and (d) a fully saturated slope with seismic forcing (Fig. 8). Results of the back analyses performed along the slopes of Tithonium and Ius Chasmata proved very similar, and revealed that dry slopes are stable (Fig. 8a), and that fully saturated slopes can produce only shallow failures of relatively small size, and cannot produce the very large slides observed in the area (Fig. 8b). Only through the application of an external horizontal force (e.g., seismic shaking caused by impact events, faulting of the crust, or volcanic activity) the entire slopes fail resulting in large to very large slides (Fig. 8c). Interestingly, the seismic effect does not trigger shallow landslides (Fig. 8c), even when the slopes are fully saturated (Fig. 8d). Instability conditions are reached with a horizontal seismic pseudo-static coefficient K_h in the range between 0.19 and 0.31, depending on the quality (GSI) of the rock mass. These coefficients correspond to horizontal PGA values in the range between 3.7 and 6.1 m s^{-2} , 1.0 to 1.6 times the local surface gravity acceleration on Mars, respectively. We acknowledge that different processes may have caused the horizontal forcing necessary to trigger the landslides, including faulting, volcanic activity, and impact events.

5. Discussion

The systematic geomorphological analysis of a 10^5-km^2 area in VM, Mars, allowed us to recognise, map, and classify a large number (219) of mass wasting features, and to prepare an accurate landslide inventory showing 198 landslides. We consider the inventory statistically complete for landslides with $A_L > 1.5 \times 10^6 \text{ m}^2$ (Table 1.S in the Supplementary material lists the measurements for the mapped landslides). Visual inspection of the new landslide inventory map (Fig. 2a) reveals that slope failures are larger in Ius Chasma than in Tithonium Chasma. In both chasmata landslides are arranged in girdles. We consider this a piece of evidence for the lateral continuity of the geological conditions that have favoured slope instability, and of a single trigger, or trigger type, for the landslides. In Ius Chasma landslides originated primarily from the northern slopes of the canyon, whereas in Tithonium Chasma the slope failures are equally abundant along the southern and the northern slopes of the canyon. Given that the morphology (e.g., height, length, gradient) of the northern and the southern slopes are similar, we conclude that the difference is indicative of local variations in the lithology and the geological structures (e.g., layers, faults, joints, cleavages, fractures).

Our classification of the mapped mass movements based on terrestrial analogues has shown that debris flows (DF) are the most abundant (41%) type of mass movements in the study area (Table 1), followed by rock slides (RS) and complex landslides (CL) that collectively account for 38% of the mapped landslides. Inspection of the probability density distribution of landslide area $p(A_L)$ for a subset of 82 landslides of the RS and CL types (Fig. 4a), and for the entire data set of 189 landslides (Fig. 4b) reveals that the mapped Martian landslides are larger than analogous terrestrial subaerial slope failures. On Earth, subaerial landslides are in the range of $10^0 \text{ m}^2 < A_L < 10^8 \text{ m}^2$ (Guzzetti et al., 2012), including the Naschitti landslide ($A_L = 4 \times 10^8 \text{ m}^2$) in the New Mexico data set, which is similar in shape and size to some of the landslides mapped in the VM. On Mars, individual landslides can be larger than 10^9 m^2 . The probability density distribution of landslide volume $p(V_L)$ confirms that Martian landslides are larger than subaerial terrestrial landslides (Fig. 5), and in the range of the largest submarine landslides, for which $V_L = 5 \times 10^{12} \text{ m}^3$ (Locat and Lee, 2009; Ten Brink et al., 2006). Analysis of the distribution of terrain gradient in the mapped landslides ($\mu = 11^\circ$, $\sigma = 9^\circ$ for all landslides, and $\mu = 7.8^\circ$, $\sigma = 5.9^\circ$ for large landslides) suggests that the Martian failures formed in a sub aerial environment.

In Fig. 4b, the probability density of landslide area $p(A_L)$ exhibits a tail for $A_L > 10^7 \text{ m}^2$ with a scaling exponent $\alpha = -1.35 \pm 0.01$ which is lower (in absolute value) than the typical scaling observed for the terrestrial landslides (Van Den Eeckhaut et al., 2007). This indicates that the proportion of very large landslides (i.e., $A_L > 10^7 \text{ m}^2$), compared to the small and the medium size failures, is significantly larger on Mars than on Earth. We hypothesise that this is due to a larger spacing of discontinuities prevailing in the Martian bedrock than on Earth. Stark and Guzzetti (2009) have shown that the scaling parameter α is a function of dimensionless cohesion of the material, or cohesive strength-to-weight ratio. The distinct difference observed in the scaling of the power law tails of terrestrial and VM landslides points to differences in the mechanical (lack of cohesion) properties of the materials involved by the slope failures. In Fig. 4b, the $p(A_L)$ for the landslides in VM does not exhibit a rollover for the small and very small landslides. For complete data sets of terrestrial landslides (e.g., landslides in Umbria, purple line in Figs. 4a and 4b), the rollover in the $p(A_L)$ for very small landslides is real, whereas for incomplete data sets (e.g., the New Mexico landslides, green line in Figs. 4a and 4b) the rollover is an artefact due to a censoring effect introduced by the partial mapping of small and very small landslides (Stark and Hovius, 2001; Malamud et al., 2004). For complete terrestrial data sets, the shape of the $p(A_L)$ is attributed to the mechanical properties of the materials that have failed as shallow or deep-seated landslides (Katz and Aharonov, 2006; Stark and Guzzetti, 2009). On Earth, lack of a distinct rollover for small landslides is considered indicative of incompleteness of the landslide data set (Stark and Hovius, 2001; Guzzetti et al., 2002). Visual analysis of high-resolution images taken by the CTX camera ($\sim 6 \text{ m/pixel}$) confirmed the presence of small and very small shallow landslides along the slopes of the chasmata, chiefly rock falls, debris slides, and debris avalanches with $A_L < 10^3 \text{ m}^2$. Analysis of the same high-resolution images revealed a systematic scarcity of medium size landslides ($10^5 \text{ m}^2 < A_L < 10^7 \text{ m}^2$) along the same slopes of the chasmata. We note that the resolution of the CTX images ($\sim 6 \text{ m/pixel}$) is sufficient to detect and map landslides in this range of areas, should the slope failures exist along the slopes of the two chasmata. We conclude that the shape of the $p(A_L)$ for Martian landslides with $A_L < 10^6 \text{ m}^2$ is the result of the real distribution of landslides in the study area, and we hypothesise that the lack of medium size landslides along the slope of the chasmata is the result of the lack of a

cohesive soil cover mantling the slopes (Katz and Aharonov, 2006; Katz et al., 2014), and to the large spacing of the discontinuities in the bedrock (layers, faults, joints, cleavages, fractures) that has favoured the formation of large and very large slope failures (Katz and Aharonov, 2006). The result of our slope stability analyses (Fig. 8) further confirms that the medium-size landslides are not probable in the study area.

The empirical relationship linking the area and the volume of the mapped Martian landslides is well described by a power law (Fig. 6). The exponent of the power law relationship (1.25 ± 0.03) is also similar to the exponents found for terrestrial landslides (Guzzetti et al., 2009; Larsen et al., 2010).

The Heim's ratio between the landslide fall height H_L and the landslide run-out distance L_L gives a measure of the apparent friction angle of the failed materials. We acknowledge that the apparent friction angle is different from the effective friction angle, as shown by Lucas and Mangeney (2007). The values measured in this work for unconfined landslides (Fig. 7) exhibit a better linear correlation, compared to other published data for terrestrial (Legros, 2002; De Blasio, 2011) and Martian (Quentin et al., 2004a) landslides. We attribute the improved correlation to a better mapping of the landslides, a result of the higher resolution of the images used to recognise and map the landslides, and the systematic application of the visual interpretation criteria. The calculated landslide apparent friction angle $\varphi = 14.4^\circ \pm 0.4^\circ$ is in the range of values reported by Schultz (2002) for wall (bedrock) rocks, and in the interval obtained from data listed in Quentin et al. (2004a).

Slope stability analyses performed along two representative topographic profiles in Tithonium and Ius Chasmata (Fig. 8) confirmed that the geometry of the most probable failure planes is similar to the geometry of large terrestrial subaerial block slides (Cruden and Varnes, 1996; Bigot-Cormier and Montgomery, 2007). On Earth, deep-seated block slides form where two (or more) sets of discontinuities are present in the bedrock. Most typically, the discontinuities are represented by a sub-horizontal or slightly dipping set comprising weak bedding planes or foliation, and a sub-vertical or inclined set comprising single or multiple joints or faults. Alternatively, deep-seated block slides form where resistant rock bridges in a hard rock fail forming a single complex shear plane. In the VM, both mechanisms are possible. Stacked volcanic rocks comprising hard lava flows and relatively weak ash fall deposits form the walls of the VM (McEwen et al., 1999; Schultz, 2002; Bigot-Cormier and Montgomery, 2007). Locally, layers or patches of weak evaporites may be interstratified with the volcanic rocks. The volcanic rocks provide a number of sub-horizontal or slightly dipping shear surfaces along which the deep-seated block slides may have formed. Evaporites, where present, may also provide weak sub-horizontal shear surfaces that can facilitate deep-seated landsliding. Distinct trenches are present on the flat uplands bounding the VM, including near some of the largest deep-seated block slides (Fig. 2a). These trenches may be the surface expression of normal faults, or they may be related to dissolution of soluble rocks at depth (Boston, 2004; Williams et al., 2010). In both cases, the trenches are the surface evidences of deep-seated, sub-vertical or inclined joint and/or fault systems along which the block slides can form. Instability conditions are reached with horizontal seismic pseudo-static coefficients corresponding to horizontal PGA values in the range between 3.7 and 6.1 m s^{-2} . This suggests that the large deep-seated slides in Tithonium and Ius chasmata were triggered by strong seismic activity, induced e.g., by impact events, faulting in the crust, or volcanic activity.

6. Conclusions

We conducted an investigation of mass wasting features in Valles Marineris, Mars, where we identified and mapped 198 landslides and 21 rock glacier-like features. This is the first systematic and statistically complete (at least, for $A_L > 1.5 \times 10^6 \text{ m}^2$) mapping and classification of landslides in VM involving a larger number of failures than previously identified in the same general area (e.g., Quentin et al., 2004a). In-depth analysis of the landslide area and volume distributions indicates that Martian landslides are larger than subaerial terrestrial landslides, and that the abundance of very large landslides ($A_L > 10^7 \text{ m}^2$), compared to small and medium area failures, is higher on Mars than on Earth. A paucity of medium size landslides ($10^5 \text{ m}^2 < A_L < 10^7 \text{ m}^2$) along the slope of the chasmata is also revealed. These findings are indicative of larger spacing fragmentation of the Martian bedrock in the VM area, likely related to the cohesion of the materials and to the landslide triggering mechanism. From back analyses of the failed slopes, we conclude that the large landslides in the Valles Marineris are most probably seismically induced, independently from dry or fully saturated conditions.

Acknowledgements

F.F. was supported by a grant of the Italian Space Agency (MORFEO project, grant number: CGS n. 2092A/08/05). M.S. was supported by a grant of the Regione dell'Umbria. P.M. was supported by a grant of the Italian Space Agency (grant number: ASI-INAF I/022/10/0). We thank K. Goto for suggestions on the use of the THEMIS and MOLA data.

Appendix A. Supplementary material

Supplementary material related to this article can be found online at <http://dx.doi.org/10.1016/j.epsl.2014.08.025>.

References

- Antonini, G., Ardizzone, F., Cardinali, M., Galli, M., Guzzetti, F., Reichenbach, P., 2002. Surface deposits and landslide inventory map of the area affected by the 1997 Umbria-Marche earthquakes. *Boll. Soc. Geol. Ital.* 121 (2), 843–853.
- Ashford, S., Sitar, N., 2002. Simplified method for evaluating seismic stability of steep slopes. *J. Geotech. Geoenviron. Eng.* 128 (2), 119–129.
- Bigot-Cormier, F., Montgomery, D.R., 2007. Valles Marineris landslides: evidence for a strength limit to Martian relief? *Earth Planet. Sci. Lett.* 260, 179–186. <http://dx.doi.org/10.1016/j.epsl.2007.05.028>.
- Borselli, L., 2013. Advanced 2D Slope stability Analysis by LEM by SSAP software: a full freeware tool for teaching and scientific community. In: Sassa, K., He, B., McSaveney, M., Nagai, O. (Eds.), *ICL Landslide Teaching Tools*. ISBN 978-4-9903382-2-0, p. 428.
- Borselli, L., 2014. SSAP 4.3.2 – Slope Stability Analysis Program. Manuale di riferimento del codice SSAP Versione 4.3.2. <http://www.ssap.eu/manualessap2010.pdf> (last accessed 17 February 2014) (in Italian).
- Borselli, L., Capra, L., Sarocchi, D., De la Cruz-Reyna, S., 2011. Flank collapse scenarios at Volcán de Colima, Mexico: a relative instability analysis. *J. Volcanol. Geotherm. Res.* 208 (1), 51–65.
- Boston, P.J., 2004. Extraterrestrial caves. In: Gunn, J. (Ed.), *Encyclopedia of Cave and Karst Science*. Fitzroy-Dearborn Publishers, Ltd., London, pp. 355–358.
- Boutrup, E., Lovell, C.W., 1980. Searching techniques in slope stability analysis. *Eng. Geol.* 16, 51–61.
- Brunetti, M.T., Guzzetti, F., Rossi, M., 2009. Probability distributions of landslide volumes. *Nonlinear Process. Geophys.* 16, 179–188. <http://dx.doi.org/10.5194/npg-16-179-2009>.
- Brunetti, M.T., Komatsu, G., Mancinelli, P., Goto, K., Santangelo, M., Saito, H., Fiorucci, F., Cardinali, M., Guzzetti, F., 2011. Detection, mapping, classification, and statistics of mass movements on Mars. Vienna, Austria. EGU General Assembly 2011, A213 (EGU2011-5750), April.
- Cardinali, M., Guzzetti, F., Brabb, E.E., 1990. Preliminary map showing landslide deposits and related features in New Mexico. U.S. Geological Survey Open File Report 90/293, 4 sheets, scale 1:500,000.

- Cardinali, M., Ardizzone, F., Galli, M., Guzzetti, F., Reichenbach, P., 2000. Landslides triggered by rapid snow melting: the December 1996–January 1997 event in Central Italy. In: Claps, P., Siccaldi, F. (Eds.), Proc. 1st Plinius Conf., Maratea. Bios Publisher, Cosenza, pp. 439–448.
- Chowdhury, R., Flentje, P., Bhattacharya, G., 2009. Geotechnical Slope Analysis. CRC Press, The Netherlands, ISBN 978-0-415-46974-6, p. 762.
- Christensen, P.R., Jakosky, B.M., Kieffer, H.H., Malin, M.C., McSween, H.Y., Nealson Jr., K., Mehall, G.L., Silverman, S.H., Ferry, S., Caplinger, M., Ravine, M., 2004. The Thermal Emission Imaging System (THEMIS) for the Mars 2001 Odyssey Mission. *Space Sci. Rev.* 110, 85–130. <http://dx.doi.org/10.1023/B:SPAC.0000021008.16305.94>.
- Crosta, G.B., Frattini, P., Valbusza, E., 2013. A New Inventory of Martian Landslides. In: 44th Lunar and Planetary Science Conference, p. 2283.
- Cruden, D.M., Varnes, D.J., 1996. Landslide types and processes. In: Turner, A.K., Schuster, R.L. (Eds.), Landslides, Investigation and Mitigation. In: Transportation Research Board Special Report 247. Washington D.C., pp. 36–75.
- Dade, W.B., Huppert, H.E., 1998. Long-runout rockfalls. *Geology* 26, 803–806. <http://dx.doi.org/10.1130/0091-7613>.
- Davies, T.R.H., 1982. Spreading of rock avalanche debris by mechanical fluidization. *Rock Mech. Rock Eng.* 15, 9–24.
- De Blasio, F.V., 2011. Landslides in Valles Marineris (Mars): a possible role of basal lubrication by sub-surface ice. *Planet. Space Sci.* 59, 1384–1392. <http://dx.doi.org/10.1016/j.pss.2011.04.015>.
- Duncan, J.M., 1996. State of the Art: limit equilibrium and finite-element analysis of slopes. *J. Geotech. Eng.* 122 (7), 577–596.
- Guzzetti, F., Malamud, B.D., Turcotte, D.L., Reichenbach, P., 2002. Power-law correlations of landslide areas in central Italy. *Earth Planet. Sci. Lett.* 195, 169–183. [http://dx.doi.org/10.1016/S0012-821X\(01\)00589-1](http://dx.doi.org/10.1016/S0012-821X(01)00589-1).
- Guzzetti, F., Ardizzone, F., Cardinali, M., Galli, M., Reichenbach, P., Rossi, M., 2008. Distribution of landslides in the Upper Tiber River basin, central Italy. *Geomorphology* 96, 105–122. <http://dx.doi.org/10.1016/j.geomorph.2007.07.015>.
- Guzzetti, F., Ardizzone, F., Cardinali, M., Galli, M., Rossi, M., Valigi, D., 2009. Landslide volumes and landslide mobilization rates in Umbria, central Italy. *Earth Planet. Sci. Lett.* 279, 222–229. <http://dx.doi.org/10.1016/j.epsl.2009.01.005>.
- Guzzetti, F., Mondini, A.C., Cardinali, M., Fiorucci, F., Santangelo, M., Chang, K.T., 2012. Landslide inventory maps: new tools for an old problem. *Earth-Sci. Rev.* 112 (1–2), 42–66. <http://dx.doi.org/10.1016/j.earscirev.2012.02.001>.
- Hoek, E., Carranza-Torres, C., Corkum, B., 2002. Hoek–Brown failure criterion – 2002 edition. In: Proc. 5th North Am. Rock Mechanics Symp., Toronto 1, pp. 267–273.
- Hsü, K.J., 1975. Catastrophic debris streams (sturzstroms) generated by rockfalls. *Geol. Soc. Am. Bull.* 86 (1), 129–140.
- Imre, B., 2004. Numerical slope stability simulations of the northern wall of eastern Candor Chasma (Mars) utilizing a distinct element method. *Planet. Space Sci.* 52 (14), 1303–1319. <http://dx.doi.org/10.1016/j.pss.2004.09.001>.
- Jaumann, R., Neukum, G., Behnke, T., Duxbury, T.C., Eichentopf, K., Flohrer, J., van Gasselt, S., Giese, B., Gwinner, K., Hauber, E., Hoffmann, H., Hoffmeister, A., Köhler, U., Matz, K.-D., McCord, T.B., Mertens, V., Oberst, J., Pischel, R., Reiss, D., Ress, E., Roatsch, T., Saiger, P., Scholten, F., Schwarz, G., Stephan, K., Wählisch, M., HRSC Co-Investigator Team, 2007. The high-resolution stereo camera (HRSC) experiment on Mars Express: instrument aspects and experiment conduct from interplanetary cruise through the nominal mission. *Planet. Space Sci.* 55, 928–952. <http://dx.doi.org/10.1016/j.pss.2006.12.003>.
- Katz, O., Aharonov, E., 2006. Landslides in vibrating sand box: what controls types of slope failure and frequency magnitude relations? *Earth Planet. Sci. Lett.* 247, 280–294. <http://dx.doi.org/10.1016/j.epsl.2006.05.009>.
- Katz, O., Morgan, J.K., Aharonov, E., Dugan, B., 2014. Controls on the size and geometry of landslides: Insights from DEM computer simulations. *Geomorphology* 220, 104–113. <http://dx.doi.org/10.1016/j.geomorph.2014.05.021>.
- Komatsu, G., Geissler, P.E., Strom, R.G., Singer, R.B., 1993. Stratigraphy and erosional landforms of layered deposits in Valles Marineris, Mars. *J. Geophys. Res.* 98 (E6), 11005–11121. <http://dx.doi.org/10.1029/93JE00537>.
- Krahn, J., 2003. The 2001 R.M. Hardy lecture: the limits of limit equilibrium analysis. *Can. Geotech. J.* 40, 643–660.
- Lajeunesse, E., Quantin, C., Allemand, P., Delacourt, C., 2006. New insights on the runout of large landslides in the Valles-Marineris canyons, Mars. *Geophys. Res. Lett.* 33, L04403. <http://dx.doi.org/10.1029/2005GL025168>.
- Larsen, I.J., Montgomery, D.R., Korup, O., 2010. Landslide erosion controlled by hill-slope material. *Nat. Geosci.* 3, 247–251. <http://dx.doi.org/10.1038/NGE0776>.
- Legros, F., 2002. The mobility of long-runout landslides. *Eng. Geol.* 63, 301–331. [http://dx.doi.org/10.1016/S0013-7952\(01\)00090-4](http://dx.doi.org/10.1016/S0013-7952(01)00090-4).
- Locat, J., Lee, H., 2009. Submarine mass movements and their consequences: an overview. In: Sassa, K., Canuti, P. (Eds.), Landslides – Disaster Risk Reduction, pp. 115–142.
- Lucas, A., Mangeney, A., 2007. Mobility and topographic effects for large Valles Marineris landslides on Mars. *Geophys. Res. Lett.* 34, L10201. <http://dx.doi.org/10.1029/2007GL029835>.
- Lucas, A., Mangeney, A., Mège, D., Bouchut, F., 2011. Influence of the scar geometry on landslide dynamics and deposits: application to Martian landslides. *J. Geophys. Res.* 116, E10001.
- Lucchitta, B.K., 1978. A large landslide on Mars. *Geol. Soc. Am. Bull.* 89 (11), 1601–1609.
- Lucchitta, B.K., 1979. Landslides in Valles Marineris, Mars. *J. Geophys. Res.* 84 (B14), 8097–8113. <http://dx.doi.org/10.1029/JB084B14p08097>.
- Lucchitta, B.K., 1987. Valles Marineris, Mars: wet debris flows and ground ice. *Icarus* 72, 411–429. [http://dx.doi.org/10.1016/0019-1035\(87\)90183-7](http://dx.doi.org/10.1016/0019-1035(87)90183-7).
- Lucchitta, B.K., Clow, G.D., Geissler, P.E., McEwen, A.S., Schultz, R.A., Singer, R.B., Squyres, S.W., 1992. The canyon system on Mars. In: Kieffer, H.H., Jakosky, B.M., Snyder, C.W., Matthews, M.S. (Eds.), Mars. University of Arizona Press, pp. 453–492.
- Makdisi, F.I., Seed, H.B., 1978. Simplified procedure for estimating dam and embankment earthquake-induced deformations. *J. Geotech. Eng.* 104 (7), 849–867.
- Malamud, B.D., Turcotte, D.L., Guzzetti, F., Reichenbach, P., 2004. Landslide inventories and their statistical properties. *Earth Surf. Process. Landf.* 29 (6), 687–711. <http://dx.doi.org/10.1002/esp.1064>.
- Malin, M.C., Bell, J.F., Cantor, B.A., Caplinger, M.A., Calvin, W.M., Clancy, R.T., Edgett, K.S., Edwards, L., Haberle, R.M., James, P.B., Lee, S.W., Ravine, M.A., Thomas, P.C., Wolff, M.J., 2007. Context Camera investigation on board the Mars Reconnaissance Orbiter. *J. Geophys. Res.* 112, E05S04. <http://dx.doi.org/10.1029/2006JE002808>.
- McEwen, A.S., 1989. Mobility of large rock avalanches: evidence from Valles Marineris, Mars. *Geology* 17, 1111–1114. [http://dx.doi.org/10.1130/0091-7613\(1989\)017<1111>2.3.CO;2](http://dx.doi.org/10.1130/0091-7613(1989)017<1111>2.3.CO;2).
- McEwen, A.S., Malin, M.C., Carr, M.H., Hartmann, W.K., 1999. Voluminous volcanism on early Mars revealed in Valles Marineris. *Nature* 397, 584–586.
- Nedell, S.S., Squyres, S.W., Andersen, D.W., 1987. Origin and evolution of the layered deposits in the Valles Marineris, Mars. *Icarus* 70, 409–441. [http://dx.doi.org/10.1016/0019-1035\(87\)90086-8](http://dx.doi.org/10.1016/0019-1035(87)90086-8).
- Neuffer, D.P., Schultz, R.A., 2006. Mechanisms of slope failure in Valles Marineris, Mars. *Q. J. Eng. Geol. Hydrogeol.* 39, 227–240. <http://dx.doi.org/10.1144/1470-9236-05-042>.
- Neukum, G., Jaumann, R., the HRSC Co-Investigator, HRSC Experiment Team, 2004. The High Resolution Stereo Camera of Mars Express. In: in Wilson, A. (Ed.), Mars Express: the scientific payload. ESA, Noordwijk, The Netherlands, pp. 17–35.
- Pierson, T.C., Costa, J.E., 1987. A rheologic classification of subaerial sediment-water flows. *Geological Society of America Reviews in Engineering Geology* 7, 1–12.
- Pike, R.J., 1988. The geometric signature: quantifying landslide-terrain types from digital elevation models. *Math. Geol.* 20 (5), 491–511.
- Quantin, C., Allemand, P., Delacourt, C., 2004a. Morphology and geometry of Valles Marineris landslides. *Planet. Space Sci.* 52 (11), 1011–1022. <http://dx.doi.org/10.1016/j.pss.2004.07.016>.
- Quantin, C., Allemand, P., Mangold, N., Delacourt, C., 2004b. Ages of Valles Marineris (Mars) landslides and implications for canyon history. *Icarus* 172, 555–572. <http://dx.doi.org/10.1016/j.icarus.2004.07.016>.
- Rib, H.T., Liang, T., 1978. Recognition and identification. In: Schuster, R.L., Krizek, R.J. (Eds.), Landslide Analysis and Control: Transportation Research Board Special Report 176. National Academy of Sciences, Washington, pp. 34–80.
- Rossi, A.P., Komatsu, G., Kargel, J.S., 2000. Rock glacier-like landforms in Valles Marineris, Mars Abstract #1587. In: 31st Annual Lunar and Planetary Science Conference, Houston, Texas.
- Sarma, S.K., 1973. Stability analysis of embankments and slopes. *Geotechnique* 23 (3), 423–433.
- Sassa, K., 1999. Landslides of the World. Kyoto University Press.
- Scheidegger, A.E., 1973. On the prediction of the reach and velocity of catastrophic landslides. *Rock Mech. Rock Eng.* 5, 231–236.
- Schultz, R., 2002. Stability of rock slopes in Valles Marineris, Mars. *Geophys. Res. Lett.* 29 (19), 1932. <http://dx.doi.org/10.1029/2002GL015728>.
- Shaller, P.J., Komatsu, G., 1994. Landslides on Mars. *Landslide News* 8, 18–22.
- Siegel, R.A., Kovacs, W.D., Lovell, C.W., 1981. Random surface generation in stability analysis. *J. Geotech. Eng.* 107 (7), 996–1002.
- Silverman, B.W., 1986. Density Estimation. Chapman and Hall, London, ISBN 978-0-412-24620-3.
- Soukhovitskaya, V., Manga, M., 2006. Martian landslides in Valles Marineris: wet or dry? *Icarus* 180, 348–352. <http://dx.doi.org/10.1016/j.icarus.2005.09.008>.
- Stark, C.P., Guzzetti, F., 2009. Landslide rupture and the probability distribution of mobilized debris volumes. *J. Geophys. Res.* 114, F00A02. <http://dx.doi.org/10.1029/2008F001008>.
- Stark, C.P., Hovius, H., 2001. The characterization of landslide size-frequency distributions. *Geophys. Res. Lett.* 28 (6), 1091–1094. <http://dx.doi.org/10.1029/2000GL008527>.
- Ten Brink, U.S., Geist, E.L., Andrews, B.D., 2006. Size distribution of submarine landslides and its implication to tsunami hazard in Puerto Rico. *Geophys. Res. Lett.* 33, L11307. <http://dx.doi.org/10.1029/2006GL026125>.
- Van Den Eeckhaut, M., Poelen, J.W.A., Govers, G., Verstraeten, G., Demoulin, A., 2007. Characteristics of the size distribution of recent and historical landslides in a populated hilly region. *Earth Planet. Sci. Lett.* 256, 588–603. <http://dx.doi.org/10.1016/j.epsl.2007.01.040>.

- van Zuidam, R.A., 1985. Aerial photo-interpretation in terrain analysis and geomorphologic mapping. International Institute for Aerospace Survey and Earth Sciences (ITC). Smits Publishers, The Hague. 442 pp.
- Venables, W.N., Ripley, B.D., 2002. Modern Applied Statistics with S. Springer, New York.
- Williams, K.E., McKay, C.P., Toon, O.B., Head, J.W., 2010. Do ice caves exist on Mars? *Icarus* 209 (2), 358–368. <http://dx.doi.org/10.1016/j.icarus.2010.03.039>.
- Zhu, D.Y., Lee, C.F., Quian, Q.H., Chen, G.R., 2005. A concise algorithm for computing the factor of safety using the Morgenstern–Price method. *Can. Geotech. J.* 42, 272–278. <http://dx.doi.org/10.1139/T09-124>.
- Zuber, M.T., Smith, D.E., Solomon, S.C., Muhleman, D.O., Head, J.W., Garvin, J.B., Abshire, J.B., Bufton, J.L., 1992. The Mars observer laser altimeter investigation. *J. Geophys. Res.* 97 (E5), 7781–7797. <http://dx.doi.org/10.1029/92JE00341>.